

The trend of disruption in the functional brain network topology of Alzheimer's disease

Alireza Fathian

Tarbiat Modares University

Yousef Jamali (✉ y.jamali@modares.ac.ir)

Tarbiat Modares University

Mohammad Reza Raoufy

Tarbiat Modares University

Research Article

Keywords: Alzheimer's disease (AD), cognitive dysfunction, functional brain network topology

Posted Date: April 21st, 2021

DOI: <https://doi.org/10.21203/rs.3.rs-440491/v1>

License: © ⓘ This work is licensed under a Creative Commons Attribution 4.0 International License.

[Read Full License](#)

The trend of disruption in the functional brain network topology of Alzheimer's disease

Alireza Fathian¹, Yousef Jamali^{1,*}, and Mohammad Reza Raoufy²

¹Biomathematics Laboratory, Department of Applied Mathematics, School of Mathematical Science, Tarbiat Modares University, Tehran, Iran

²Department of Physiology, Faculty of Medical Sciences, Tarbiat Modares University, Tehran, Iran

*y.jamali@modares.ac.ir

ABSTRACT

Alzheimer's disease (AD) is a progressive disorder associated with cognitive dysfunction that alters the brain's functional connectivity. Assessing these alterations has become a topic of increasing interest. However, a few studies have examined different stages of AD from a complex network perspective that cover different topological scales. This study analyzed the trend of functional connectivity alterations from a cognitively normal (CN) state through early and late mild cognitive impairment (EMCI and LMCI) and to Alzheimer's disease. The analyses had been done at the local (hubs and activated links and areas), meso (clustering, assortativity, and rich-club), and global (small-world, small-worldness, and efficiency) topological scales. The results showed that the trends of changes in the topological architecture of the functional brain network were not entirely proportional to the AD progression, and these trends behaved differently at the earliest stage of the disease, i.e., EMCI. Further, it has been indicated that the diseased groups engaged somatomotor, frontoparietal, and default mode modules compared to the CN group. The diseased groups also shifted the functional network towards more random architecture. In the end, The methods introduced in this paper enable us to gain an extensive understanding of the pathological changes of the AD process.

Introduction

Alzheimer's disease is an irreversible and progressive brain disorder that is the fifth cause of death worldwide and does not have a pharmacological treatment for cure or prevention^{1,2}. AD progression can be considered as a continuum from the cognitively normal state through early and late mild cognitive impairment to Alzheimer's disease, characterized by the loss of memory and cognitive dysfunction. In more detail, it has been shown that the transition probabilities from MCI to more severe states of AD at age 65 is 14% higher than the transition from CN, and this likelihood is increasing by age³. Moreover, the studies show that these disorders are associated with dysfunction in the whole brain neural connectivity rather than a local brain region⁴⁻⁶. Therefore, a non-invasive and computational method for modeling the connectivity across the whole brain can help to understand the alterations in the brain network architecture corresponding to the disease progression and provide an opportunity for early diagnosis and understanding of the disease process. In this regard, the use of graph-theoretical methods and complex network theory for modeling the brain as an interconnected network of brain regions have been a focus of interest in recent years^{7,8}. In most of the studies, the general framework for developing the brain networks include the selection of spatial and temporal scale and resolution of the study data⁹⁻¹³, the appropriate atlases that divide the brain into distinct regions¹⁴, the type of connection among regions (anatomical, functional, or effective connectivity)^{15,16}, and finally the methods of estimating these connectivities¹⁷⁻¹⁹.

Resting-state functional magnetic resonance imaging (rs-fMRI), which measures the neural activity in the resting state based on the blood-oxygen-level-dependent (BOLD) contrast, has been widely used to estimate the functional connectivity network of the brain^{20,21}. Studies indicate the emergence of several complex network phenomena such as assortativity^{22,23}, rich-club^{24,25}, clustering^{26,27}, and small-world^{28,29} in these networks. The modularity and the importance of hub regions have also been discussed in several studies³⁰⁻³². Further, considering the sensitivity of these networks to brain disorders³³⁻³⁵, many studies have aimed to develop computational methods for diagnosing and understanding of the disease process³⁶⁻³⁸. Specifically, in the case of AD and its early stages, many studies reported the disturbance of the functional network architecture, indicating the disappearance of rich-club³⁹, clustering⁴⁰, and small-world^{41,42} phenomena, and alterations in the spatial distribution of the hub regions (high ranked regions)^{43,44}. However, to the best of our knowledge, none of the studies have done a comprehensive comparative assessment of the functional brain network of patients with AD and its early stages that include all of those subjects mentioned above.

The human brain has an intrinsic multi-scale architecture⁴⁵, which is emerged in different aspects of the data: spatial, temporal, and topological aspects¹³. In this study, the alterations in the human brain functional connectivity network corre-

sponded to the progression of the disease from CN through EMCI and LMCI, and to AD were assessed using multi-scale topological analysis. For each study group, a functional connectivity network of 360 brain regions was computed. The results of different analyses that have been done on these networks are divided into three topological scales: analyses at the scale of the whole network (global), analyses at the single vertex scale (local), and analyses that are in between local and global scales (mesoscale)¹³.

The core question throughout this paper is whether these alterations are following a trend proportional to the disease progression in the continuum from CN to AD. The presence of such trends is perceptible in most of the results in this study. However, in some of them, the trends are not entirely proportional to the disease progression and behave differently in the early stages of the AD spectrum. Further, the analysis showed that the functional brain network tends to shift toward a more randomized architecture by the disease progression. Also, it has been observed that the frontoparietal, somatomotor, and default mode modules are affected more than other modules introduced in the next section.

Results

The results of this study are mainly obtained from the comparative analysis of 4 study networks, each representing a study group's functional connectivity network. In order to construct these networks, the fMRI and T1-weighted (T1w) images of 92 subjects (23 subjects for each study group) were passed through a processing pipeline that includes the preprocessing using *fMRIPrep* 20.0.0 (^{46, 47}, RRID:SCR_016216), extracting 36 nuisance regressors, parcellating the brain surface area into 360 regions, constructing connectivity network among these regions with Pearson correlation coefficient (PCC), computing the mean of the networks that belong to subjects within each study group, and finally, thresholding these four mean networks. The overall processing pipeline can be found in Supplementary Fig. S1.

Global network analysis

Significant differences were revealed at the global level analysis. The PCC and the Jaccard similarity coefficient are measures for evaluating the correlation and the similarity among two vectors. Computing these measures among vectorized adjacency matrices (a matrix that use to represent a network, where the value of the element (i, j) of this matrix equals the weight of the link between the vertices i and j .) corresponded to the 4 study networks were showed that the similarity between the CN network and disease networks were decreased by the progression of the disease (Fig. 1 a and c). However, the existence of similarity between the brain networks of the subjects belong to the same study group was still unclear. To obtain a more reliable comparison that takes into account these similarities, the samples of each study group were randomly divided into two subgroups of 12 and 11 samples. Similar to the process explained in the "Methods" section for computing the mean network of each study group based on its 23 samples, two different mean networks were generated for each study group based on these two subgroups of samples. Then, PCC and the Jaccard similarity coefficient among the 11-samples mean networks and the 12-samples mean networks were computed. This process was repeated 100 times, resulting in 100 similarity matrices for each of the mentioned similarity measures. Then, the element-wise mean and standard deviation (SD) over these matrices were computed, and the results showed the existence of almost similar trends (Fig. 1 b and d). Further, as seen in Fig. 1, SD is increasing by the disease progression, which means that the similarity coefficients become more inconsistent in the course of the disease.

The mean and SD of vertex strength (the total weight of the vertex connections) also had a decreasing trend. Furthermore, the links were classified into short and long links based on their euclidean length (the short (long) links were defined as the links that the euclidean distance between its vertices is smaller (larger) than the average distance among all vertices.). For each study network, the proportion of the average weight of the long links to the average weight of the short links was computed. As it is shown in table 1, this value is decreasing with the progression of the disease.

There was also an inverse relationship between the local and global efficiency, which are measures for the efficiency of information exchange over the networks. The global efficiency measures the information exchange over the whole network, whereas the local efficiency measures the fault-tolerant of the network by quantifying the information exchange between the neighbors of each vertex when that vertex is removed⁴⁸. While local efficiency in the CN group was higher than other groups, global efficiency in the CN group was lower than LMCI and AD groups (Fig. 2d).

The small-world (six degrees of separation) phenomenon describes that it is possible to reach any network vertex from other vertices by passing through a small chain of connected vertices. It has been shown that in small-world networks, the average shortest path length ($\langle l \rangle$) grows logarithmically with the network size. This phenomenon can be evaluated by measuring $\langle l \rangle$ and the growth rate of the average number of vertices within a distance less than or equal to l from any given vertex ($M(l)$). It has been shown that in small-world networks, $M(l)$ is increasing faster than the exponential growth⁴⁹. The $M(l)$ function plotted in Fig. 2a and the values of $\langle l \rangle$, shown in Fig. 2b, both suggest that the study networks have the small-world property. However, these figures indicate that similar to the global efficiency shown in Fig. 2d; the changing patterns are not quite proportional to the disease progression. Specifically, in almost all of the figures mentioned above, the only study group

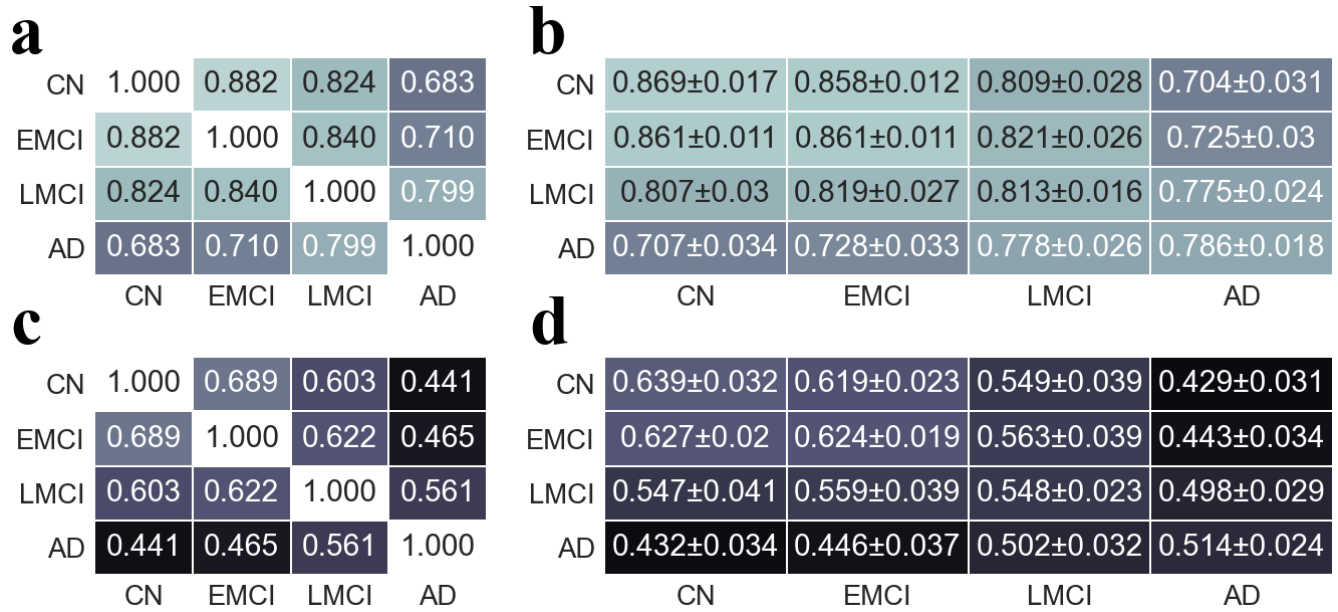


Figure 1. The similarity between study groups follows a trend proportional to the trend of disease progression. (a) The PCC between the four main study networks. (b) For each study group, the 23 subjects of each group were randomly divided into two subgroups of 11 and 12 networks. Then, the mean networks of these 12 and 11 subjects were constructed, and the PCC between these two mean networks was computed. This process was repeated 100 times resulting in 100 PCC matrices. This panel shows the element-wise mean and SD of these matrices. (c) The Jaccard similarity coefficient among the four main study networks. (d) Similar to the panel (b) but for the Jaccard similarity coefficient.

which is not following the expected trend is the EMCI group. The existence of the small-world phenomenon along with the high value of average clustering coefficient ($\langle C \rangle$), will lead to a more specific emergence property of complex networks called small-worldness. σ which equals the division of the normalized $\langle l \rangle$ by the normalized $\langle C \rangle$, is a measure of evaluating this new phenomenon explained in the section "Methods". Figure 2d indicates that in all networks, $\sigma > 1$, which means that they all have the small-worldness property. This figure also indicates that σ , and consequently the small-worldness, increase by the disease progression with the exception of the EMCI group, which is not following the trend.

Study Group	CN	EMCI	LMCI	AD
Total Strength	9.35 ± 5.4	7.84 ± 4.9	7.77 ± 4.5	7.56 ± 3.8
Density	0.072	0.063	0.066	0.064
Long/Short Links	0.144	0.103	0.062	0.057
Intra-module/Inter-module Links	10.741	10.659	9.668	7.338

Table 1. General information about the distribution of edges.

Mesoscale network analysis

The analysis that had been done in the mesoscale indicates the existence of trends similar to the analyses at the global scale.

Clustering, assortativity, and rich-club

The clustering, assortativity, and rich-club phenomena have been used to describe the higher-level architecture of a complex network. The high value of $\langle C \rangle$ indicates the presence of highly interconnected groups of vertices within the network. This measure which is depicted in the second bar plot of Fig. 2d, shows that the clustering phenomenon is decreasing by the disease progression. The assortativity phenomenon is characterized when neighbor vertices are likely to have similar degrees. In Fig. 2b, the increasing diagram of the average degree of the nearest neighbors for vertices of degree k ($k_{nn}(k)$) indicates the presence of this phenomenon. This figure and the last bar plot in Fig. 2d showing the PCC between the degrees of all vertices at either ends of an edge (r) in each study network, also indicate that the assortativity is disappearing by the disease progression. The rich-club phenomenon is characterized when large degree vertices are more interconnected with each other than with the

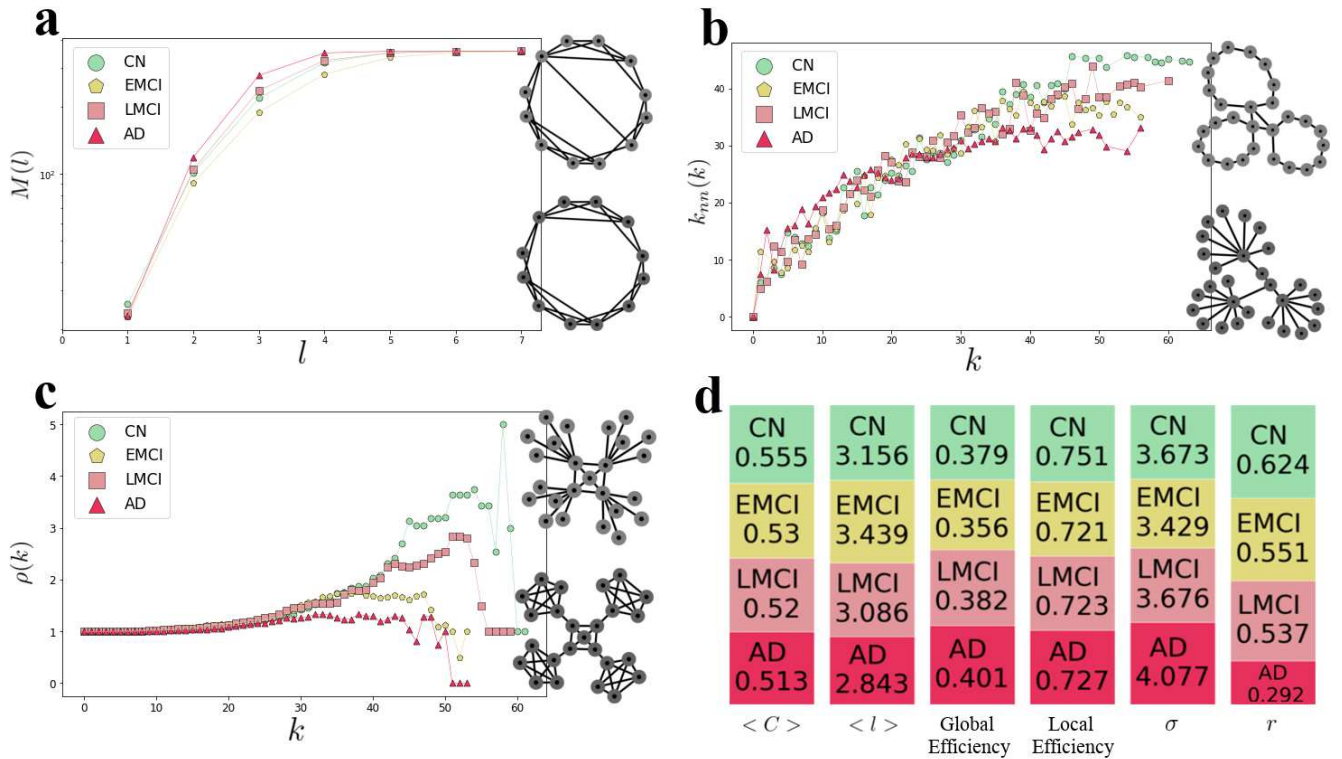


Figure 2. The emergence of the small-worldness, assortativity, and rich-club phenomenon in the study networks. (a) $M(l)$ plot showing the average number of vertices within a distance less than or equal to l from any given vertex is almost increased by the disease progression and suggests that the study networks have the small-world property that is almost stronger in the disease networks. Two graphs on the right-hand side are toy examples demonstrating the increase in the randomness of network connections (from bottom to top), which leads to the increase in the emergence of the small-world property. (b) $k_{nn}(k)$ plot showing the average degree of the nearest neighbors, for vertices of degree k , is almost decreased by the disease progression and suggests that the study networks have assortative architecture and this assortative matching follows a decreasing trend proportional to the disease progression. Two graphs on the right-hand side are toy examples of assortative (top) and disassortative (bottom) networks. (c) $\rho(k)$ plot showing the amount of inter-connectivity among vertices of degree higher than k is almost decreased by the disease progression and suggests that the rich-club phenomenon is disappearing by the disease progression. Two graphs on the right-hand side are toy examples of networks with (top) and without (bottom) rich-club. (d) The bar plots showing $\langle C \rangle$, $\langle l \rangle$, global efficiency, local efficiency, σ (normalized $\langle C \rangle$ / normalized $\langle l \rangle$), and r (PCC between the degrees of all vertices at either ends of an edge).

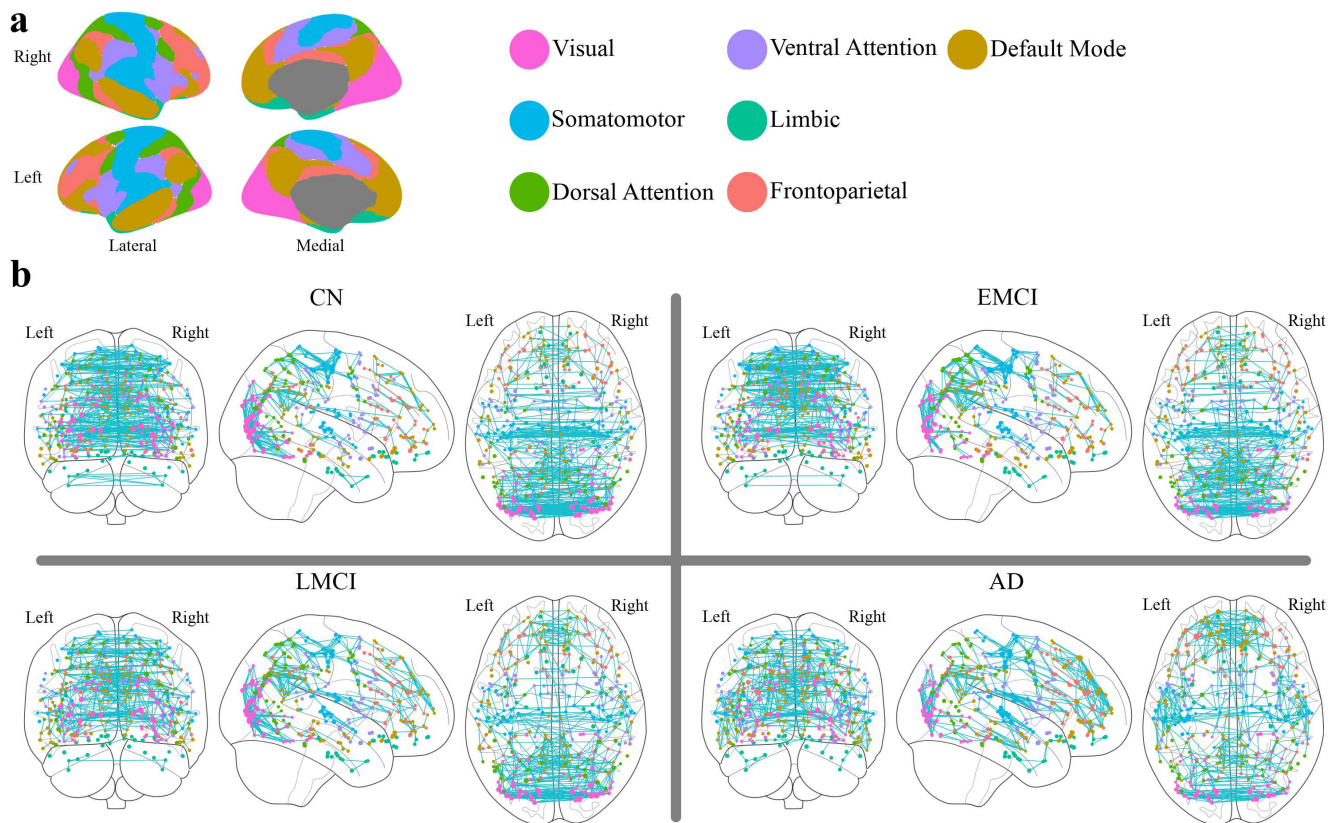


Figure 3. The overall gradually changing patterns of highly-weighted links are following a trend proportional to the disease progression. (a) The spatial distribution of the 7-module parcellation (made with “ggseg” R package⁵¹). (b) The top 1 percent highly-weighted links of each study network. Vertex color represents the module the vertex belongs to, and the vertex size is proportional to the vertex strength. It shows that there is a trend towards the increase in the number of default mode links as well as the intra-hemisphere links in limbic. It also shows a trend towards the decrease in the inter-hemisphere links in limbic and dorsal attention.

smaller degree vertices. The diagram in Fig. 2c plotting the fraction of edges connecting vertices with degree higher than k out of the maximum number of edges that these vertices can possibly share ($\rho(k)$), indicates the presence of the rich-club phenomenon, which is disappearing by the disease progression.

Modular analysis

The 360 brain regions were classified into seven modules based on a well-known parcellation provided by Yeo et al.⁵⁰ (Fig. 3a). Then, the topological architecture of intra-module and inter-module connection networks was analyzed. First, by reorganizing the position of vertices in each study network’s adjacency matrix based on this classification, the existence of a substantial structure that was disappearing with the progression of disease was observed (see Supplementary Fig. S2 online). For each study network, the proportion of the average weight of the intra-module links to the average weight of the inter-module links was computed. As it is shown in table 1, this value is decreasing with the progression of the disease. Further, for each study group, the modular sub-networks, containing the vertices belong to each module, were computed. Then, similar to the "Global network analysis" section where the PCC between adjacency matrices of the study networks was measured, for each module, the PCC was computed among the adjacency matrices of the modular sub-network of each study network, and the results showed that these modules are sensitive to the disease progression (see Supplementary Fig. S3 online).

Local network analysis

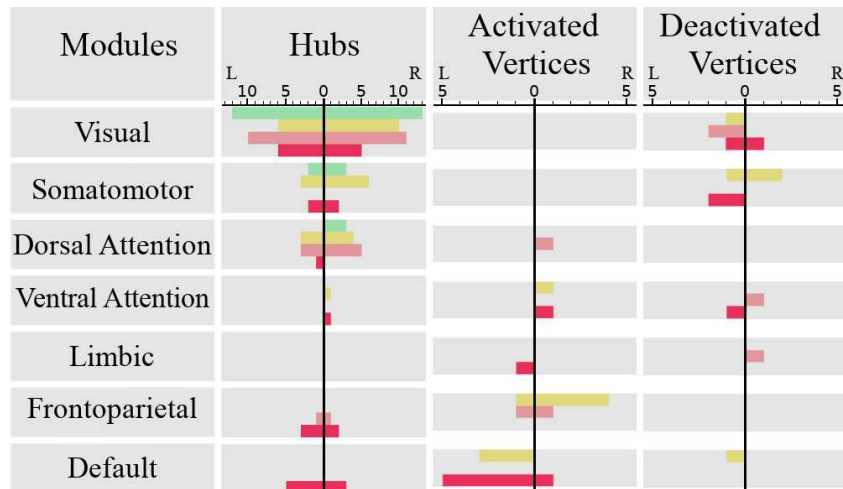
Several approaches have been attempted to attain a general conclusion about the distribution of the regions and links that are most sensitive to the disease progression at the finest topological scale.

In order to attain the most sensitive vertices, the spatial distribution of the strength-based hub vertices (high strength vertices) and the diseased-related activated and deactivated vertices were calculated (Fig. 4 b and c). Further, the frequency distribution of these vertices across the 7-module parcellation introduced in the "Modular analysis" section is shown in Fig. 4a.

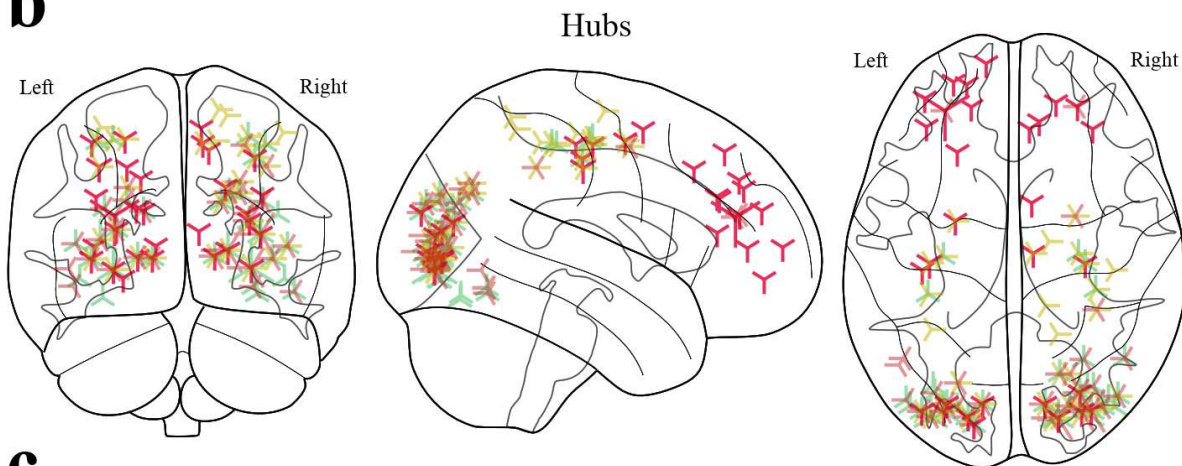
Legends

CN
EMCI
LMCI
AD
Hubs 
Activated Vertices 
Deactivated Vertices 

a



b



c

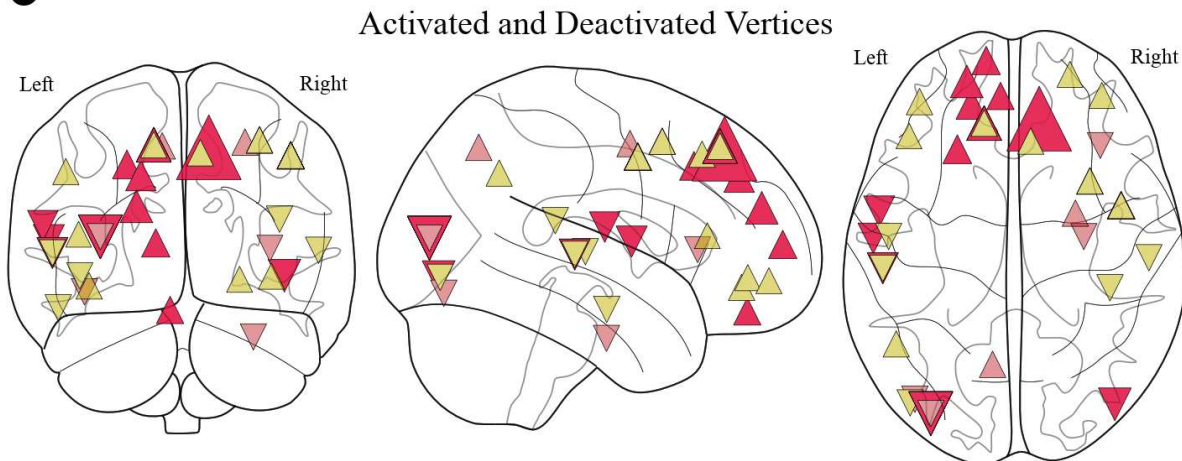


Figure 4. The distribution of hubs, activated areas, and deactivated areas shows that anterior regions are more engaged in the diseased groups. (a) The frequency distribution across the 7-module parcellation. The left and right sides of each sub-plot denoted by a vertical black line represent the distribution across modules limited to the left and right hemispheres, respectively (b) The spatial distribution of the hub regions. The vertex size is proportional to the vertex strength. (c) The spatial distribution of vertices that are activated (denoted by \triangle) and deactivated (denoted by ∇) in the diseases. A vertex was called activated (deactivated) with respect to disease if the subtraction of its strength in the disease network from the CN network was significantly larger (smaller) than the similar value for other vertices. The vertex size is proportional to the value of this subtraction.

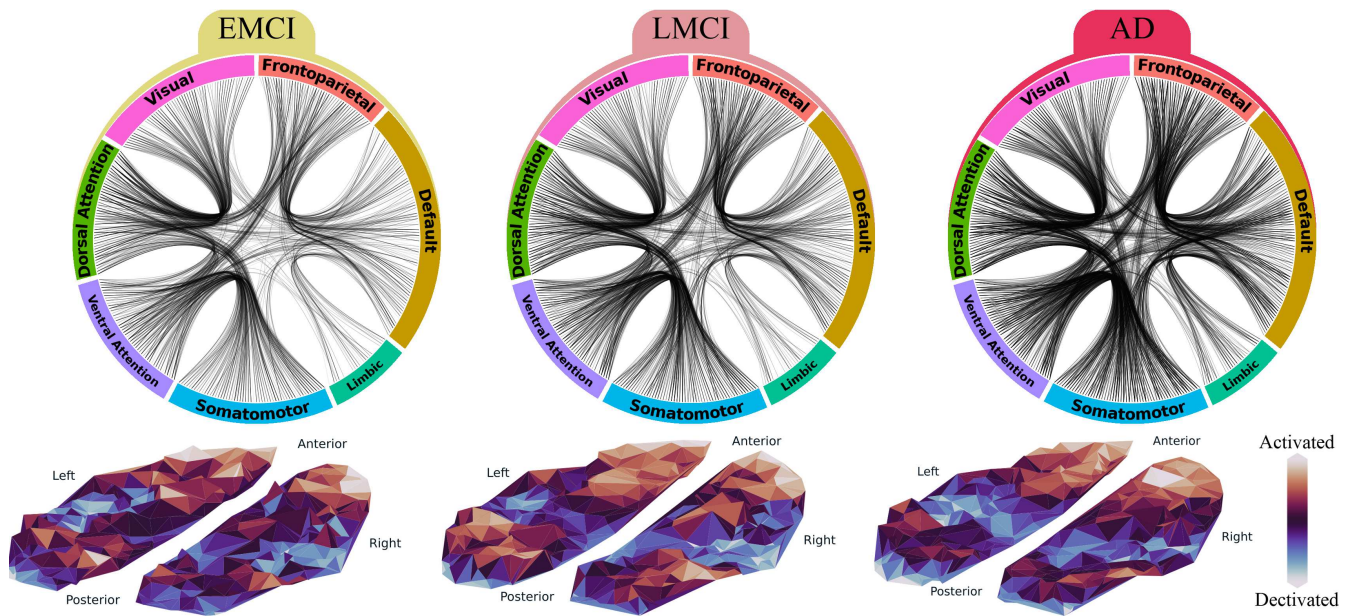


Figure 5. The alterations in the brain functional network induced by the disease stages. For each disease stage the connectogram of the links with significantly different weights as compared to the CN group is depicted in the top row. It shows a similar inter-module connectivity pattern is repeating through all disease stages. The altered links with respect to disease are defined as the significantly larger or smaller elements of the matrix results from the subtraction of the disease network from the CN network. Diagrams are plotted based on the *Hierarchical Edge Bundling* algorithm⁵², which allows bundling the intra-module edges together to get a more elegant presentation. The bottom row indicates the alterations in the vertices' strength by showing the top-view spatial distribution of the activated or deactivated vertices similar to Fig. 4c.

In order to attain the most sensitive edges, for each disease stage a network including the significantly altered links in the diseased network with respect to the CN network was constructed. As it is obvious in Fig. 5, These networks show a similar connectivity pattern among the seven modules, which is becoming more and more apparent by disease progression.

In order to attain the strong connections among modules in the mentioned pattern, for each disease stage, the average weight of the altered links that connect vertices belonging to each pair of modules was calculated. Interestingly, the top 10 pairs of modules were similar in all altered networks of the disease stages, showing the connections among ventral attention and somatomotor, dorsal attention and visual, frontoparietal and default mode, dorsal attention and somatomotor, dorsal attention and ventral attention, dorsal attention and frontoparietal, ventral attention and frontoparietal, default mode and somatomotor, limbic and default mode, and default mode and ventral attention modules. Also, the overall gradually changing pattern of the top 1 percent highly-weighted links of the study networks is depicted in Fig. 3b. It shows a changing pattern toward increasing the number of default mode links and the intra-hemisphere links in limbic. It also shows a changing pattern toward decreasing the inter-hemisphere links in limbic and dorsal attention modules.

Discussion

The main goal of this study was to investigate the alterations of the brain functional network topology in patients with AD, LMCI, and EMCI compared to the CN patients from a multi-scale topological perspective. This study attempted to find quantitative network measures that are proportional to the trend of brain deterioration from CN patients through AD in order to suggest network-based biomarkers and also help to understand the disease process. There are three general findings in this study. First, the functional brain network constructed in this study is sensitive to the progression of AD. Second, the functional brain network of the diseased groups tends to shift towards a more randomized and integrated architecture. Third, the present study suggests that the alterations in the network architecture may not be entirely proportional to the disease progression. In this regard, the functional brain network architecture may go through a nonlinear process and behave differently in earlier stages in the course of the disease progression.

Several study results suggested that the networks of the disease groups have larger global efficiency. These results include the increase in the global efficiency, the small-world property, and the proportion of inter-module to intra-module link weights. There are also several results suggesting the smaller local efficiency. These results include the decrease in the local efficiency,

$\langle C \rangle$, and the proportion of intra-module to inter-module link weights. This inverse relationship which is reported by previous brain studies^{53,54} can be explained by considering the increase of global efficiency as a compensatory mechanism for the decrease in the local efficiency. This will lead to the efficiency in information spreading across the whole brain but the loss of efficacy in information spreading in the finer scales of vertices and their neighbors. Considering the sparse nature of the brain networks, the increase in the global and decrease in the local efficiency indicate that the disease networks have a more random organization.

The analysis at the mesoscale revealed the alteration in the brain network organization in a way that causes the disappearance of the assortative mixing and the rich-club phenomenon. $\rho(k)$ is declining by the disease progression, and in the case of the AD network, it is around 1 in almost everywhere, which means that the brain network tends to behave more similarly to random networks. This significant rich-club reorganization magnifies the importance of analyzing the alterations of the hub regions. The diseased networks' hubs are more distributed over the modules, and it is consistent with the claim that the diseased networks are more randomized and integrated. Furthermore, the diseased groups have significantly more hubs located in anterior regions as compared to the CN group. In more detail, the analysis of activated and deactivated areas shows that the default mode, frontoparietal, and somatomotor modules have significantly affected by the disease. As suggested by Sha et al.⁵⁵, this observation can find its explanation in the functionality of these modules: frontoparietal is responsible for cognitive control, the default mode network is involved in internal emotional processing, self-referential directed thought, and memory function⁵⁵, and somatomotor is responsible for motor skill learning and sensory perception. Furthermore, As it is also reported by other studies^{56,57}, in addition to these modules, the dorsal and ventral attention, which are respectively involved in the top-down and bottom-up attention process, are also significantly involved in the networks of the disease-related alterations.

Despite several advantages in this study, some limitations should be addressed. First, due to the ill-posed nature of constructing functional network problems and due to the lack of ground truth in any of the main steps for generating functional networks out of neuroimaging data, many different strategies can be used for this purpose⁵⁸. Previous studies have shown that depend on the type of analysis, different strategies can lead to different results^{14,59}. Therefore, a comparative analysis of different strategies would help choose appropriate strategies depending on the different scales of topological network analysis and investigating whether a single strategy would be appropriate for all scales. Second, Because of the same reasons mentioned in the first limitation, it can be difficult to distinguish which strategy leads to the results that present a more valid biological interpretation⁵⁸. In the case of using these results for developing machine learning models, this lack of interpretability is acceptable, but interpreting these results in order to understand the disease process and the underlying mechanisms that lead to the disease, should be done more carefully.

In conclusion the analyses offered in this paper can help to gain an understanding of the topological changes in the functional brain network architecture. Most previous studies for analyzing the AD spectrum, focused on one topological scale. Using a multi-scale topological approach this paper extensively demonstrated the pathological changes of the AD process. The issues mentioned in the limitations are the subjects of future works. A comparative assessment of different functional networks constructed based on widely used strategies will help to find strategies with higher sensitivity to AD spectrum.

Methods and materials

Demographic and clinical information

Data used in the preparation of this article were obtained from the Alzheimer's Disease Neuroimaging Initiative (ADNI) database (adni.loni.usc.edu). The primary goal of ADNI has been to test whether serial magnetic resonance imaging (MRI), positron emission tomography (PET), other biological markers, and clinical and neuropsychological assessment can be combined to measure the progression of MCI and early AD. Table 2 shows the demographic and clinical information of the 92 study subjects.

Group	CN	EMCI	LMCI	AD
Number	23	23	23	23
Male, Female	8,15	12,11	10,13	11,12
Age (mean \pm SD)	75.82 \pm 9.44	75.29 \pm 6.36	72.26 \pm 7.05	77.75 \pm 3.75
MMSE (mean \pm SD)	28.96 \pm 1.17	28.32 \pm 1.89	25.87 \pm 3.86	20.32 \pm 4.26
GDSCALE (mean \pm SD)	1.04 \pm 1.41	1.80 \pm 1.85	1.94 \pm 2.29	1.37 \pm 1.32
Global CDR (mean \pm SD)	0.40 \pm 0.13	0.39 \pm 0.24	0.49 \pm 0.25	0.96 \pm 0.40
FAQ (mean \pm SD)	0.25 \pm 1.22	2.77 \pm 4.22	5.06 \pm 6.68	18.26 \pm 7.87
NPI-Q (mean \pm SD)	0.67 \pm 1.54	2.47 \pm 2.52	2.08 \pm 1.98	4.85 \pm 3.78

Table 2. Demographic and clinical information of the studied groups

Preprocessing

The neuroimaging data was preprocessed using *fMRIPrep* 20.0.0, which is based on *Nipype* 1.4.2 (^{60, 61}, RRID:SCR_002502).

Anatomical data preprocessing

The T1w image was corrected for intensity non-uniformity (INU) with ‘N4BiasFieldCorrection’⁶², distributed with ANTs 2.2.0 [⁶³, RRID:SCR_004757], and used as T1w-reference throughout the workflow. The T1w-reference was then skull-stripped with a *Nipype* implementation of the ‘antsBrainExtraction.sh’ workflow (from ANTs), using OASIS30ANTs as target template. Brain tissue segmentation of cerebrospinal fluid (CSF), white-matter (WM) and gray-matter (GM) was performed on the brain-extracted T1w using ‘fast’ [FSL 5.0.9, RRID:SCR_002823⁶⁴]. Brain surfaces were reconstructed using ‘recon-all’ [FreeSurfer 6.0.1, RRID:SCR_001847,⁶⁵], and the brain mask estimated previously was refined with a custom variation of the method to reconcile ANTs-derived and FreeSurfer-derived segmentations of the cortical gray-matter of Mindboggle [RRID:SCR_002438,⁶⁶]. Volume-based spatial normalization to one standard space (MNI152NLin2009cAsym) was performed through nonlinear registration with ‘antsRegistration’ (ANTs 2.2.0), using brain-extracted versions of both T1w reference and the T1w template. The following template was selected for spatial normalization: *ICBM 152 Nonlinear Asymmetrical template version 2009c* [⁶⁷, RRID:SCR_008796; TemplateFlow ID: MNI152NLin2009cAsym],

Functional data preprocessing

For each of the 1 BOLD runs found per subject (across all tasks and sessions), the following preprocessing was performed. First, a reference volume and its skull-stripped version were generated using a custom methodology of *fMRIPrep*. Susceptibility distortion correction (SDC) was omitted. The BOLD reference was then co-registered to the T1w reference using ‘bbrregister’ (FreeSurfer) which implements boundary-based registration⁶⁸. Co-registration was configured with six degrees of freedom. Head-motion parameters with respect to the BOLD reference (transformation matrices, and six corresponding rotation and translation parameters) are estimated before any spatiotemporal filtering using ‘mcflirt’ [FSL 5.0.9,⁶⁹]. The BOLD time-series were resampled onto the following surfaces (FreeSurfer reconstruction nomenclature): *fsaverage5*. The BOLD time-series (including slice-timing correction when applied) were resampled onto their original, native space by applying the transforms to correct for head-motion. These resampled BOLD time-series will be referred to as *preprocessed BOLD in original space*, or just *preprocessed BOLD*. The BOLD time-series were resampled into standard space, generating a *preprocessed BOLD run in MNI152NLin2009cAsym space*. First, a reference volume and its skull-stripped version were generated using a custom methodology of *fMRIPrep*. Several confounding time-series were calculated based on the *preprocessed BOLD*: framewise displacement (FD), DVARS and three region-wise global signals. FD and DVARS are calculated for each functional run, both using their implementations in *Nipype* [following the definitions by⁷⁰]. The three global signals are extracted within the CSF, the WM, and the whole-brain masks. Additionally, a set of physiological regressors were extracted to allow for component-based noise correction [*CompCor*,⁷¹]. Principal components are estimated after high-pass filtering the *preprocessed BOLD* time-series (using a discrete cosine filter with 128s cut-off) for the two *CompCor* variants: temporal (tCompCor) and anatomical (aCompCor). tCompCor components are then calculated from the top 5% variable voxels within a mask covering the subcortical regions. This subcortical mask is obtained by heavily eroding the brain mask, which ensures it does not include cortical GM regions. For aCompCor, components are calculated within the intersection of the aforementioned mask and the union of CSF and WM masks calculated in T1w space, after their projection to the native space of each functional run (using the inverse BOLD-to-T1w transformation). Components are also calculated separately within the WM and CSF masks. For each *CompCor* decomposition, the *k* components with the largest singular values are retained, such that the retained components’ time series are sufficient to explain 50 percent of variance across the nuisance mask (CSF, WM, combined, or temporal). The remaining components are dropped from consideration. The head-motion estimates calculated in the correction step were also placed within the corresponding confounds file. The confound time series derived from head motion estimates and global signals were expanded with the inclusion of temporal derivatives and quadratic terms for each⁷². Frames that exceeded a threshold of 0.5 mm FD or 1.5 standardised DVARS were annotated as motion outliers. All resamplings can be performed with a *single interpolation step* by composing all the pertinent transformations (i.e. head-motion transform matrices, susceptibility distortion correction when available, and co-registrations to anatomical and output spaces). Gridded (volumetric) resamplings were performed using ‘antsApplyTransforms’ (ANTs), interpolation to minimize the smoothing effects of other kernels⁷³. Non-gridded (surface) resamplings were performed using ‘mri_vol2surf’ (FreeSurfer).

Next, confound regression with 36-parameters (including 6 motion parameters of translation and rotation, mean signal in white matter, mean signal in cerebrospinal fluid, and global signal, as well as their derivatives, quadratic terms, and squares of derivatives) were conducted to the data resampled onto FreeSurfer *fsaverage5* surface space⁷².

Network construction

The human connectome project’s multi-modal parcellation, version 1.0 (HCP_MMP 1.0)⁷⁴ were used to parcellate each participant’s data into 360 regions. It has been shown that this parcellation is more robust and sensitive to AD progression than

many other widely used parcellations, and it is probably the most detailed cortical in-vivo parcellation available to date^{14,75}. The time series corresponding to each region is then the mean of the time series of voxels within that region. Then, the weighted undirected functional connectivity network was obtained by computing the PCC between time series of all regions. In order to obtain a single network for each study group, the mean network of each group was computed as the element-wise mean of all networks belong to the subjects within that group. Finally, using a data-driven method, the resulting networks were thresholded. For each network, we searched for a thresholding value that maximizes the global efficiency (E) minus the proportion of the strongest weights (PSW) (equation (1,2))⁷⁶.

$$E(t) = \frac{1}{n} \sum_{i \in N} \frac{\sum_{j \in N, j \neq i} (\frac{1}{d_{ij}})}{n-1} \quad (1)$$

$$PSW(t) = \frac{\sum_{i \in W, i \geq t} i}{\sum_{j \in W} j} \quad (2)$$

Where N is the set of all vertices, n is the number of vertices, d_{ij} is the shortest path length between vertices i and j , and W is the set of all weights.

Network analysis

Network efficiency

The efficiency of information exchange throughout the networks can be assessed from local and global perspectives^{48,77,78}.

Having a small $\langle l \rangle$ leads to efficient information exchange from the global point of view. Accordingly, several quantitative methods were introduced to assess this efficiency. The global efficiency, which is the inverse sum of the shortest path length among vertices, is one of them⁴⁸. The small-world property which is a common emergence phenomenon among many real-world complex network systems, also guarantees high efficiency in the information exchange from the global perspective. This measure that also calls the six degrees of separation, exists if $\langle l \rangle$ scales slower than the logarithmic growth with the size of the network. $M(l)$ is defined as the average number of vertices within a distance less than or equal to l from any given vertex. Then $M(l)$ is expected to grow faster than the exponential growth in the small-world networks⁴⁹. It has been shown that many real-world complex networks are mostly sparse networks with high $\langle C \rangle$ ⁷⁹ that will lead to the efficiency in the local information exchange. This efficiency can also be assessed by measuring the average efficiency of the sub-networks, including each vertex and its neighbors⁴⁸. Clearly, this efficiency can not be attained if the network has a completely random organization. However, the sparse nature of these networks, along with the existence of the small-world property, implies that these networks can not be like regular networks, and there should be random rearrangements in the connections of these networks to form hubs and connectivity backbones and leads to faster information exchange and decrease in $\langle l \rangle$ ⁴⁹. Therefore, the emergence of both local and global efficiency, which can be explained by the trade-off between the regular and random organization of the connections⁷⁷, was recognized as a new phenomenon, called the small-worldness⁸⁰. A straightforward approach for quantifying this phenomenon is to divide the normalized $\langle l \rangle$ by the normalized $\langle C \rangle$ ($\sigma = \langle l \rangle_{rand} / C_{rand}$). The normalization can be done by dividing the actual value of each measure by the value of the measure for a corresponding Erdős–Rényi random graph. A network is then said to have small-worldness if $\sigma > 1$ ⁸⁰.

Assortativity

The assortative property refers to the tendency of vertices to connect to other vertices with similar degree. In this study, this property was measured using two methods. First, the PCC between the degrees of all vertices on either ends of an edge was computed as:

$$r = \frac{\sum_e j_e k_e / E - [\sum_e (j_e + k_e) / (2E)]^2}{[\sum_e (j_e^2 + k_e^2) / (2E)] - [\sum_e (j_e + k_e) / (2E)]^2} \quad (3)$$

Where j_e and k_e denote the degree of the extremities of edge e and E is the total number of edges. This quantity lies in the range $-1 \leq r \leq 1$, where -1 refers to disassortative networks and 1 refers to totally assortative networks⁸¹. The second method measures the assortativity by computing the average degree of the nearest neighbors, for vertices of degree k ($k_{nn}(k)$).

$$k_{nn}(k) = \frac{1}{N_k} \sum_{i/k_i=k} k_{nn,i} \quad (4)$$

Where N_k is the number of vertices with degree k and $k_{nn,i}$ is the average degree of the nearest neighbors, for the vertex i . If $k_{nn}(k)$ is an increasing function of k , the average degree of the nearest neighbors, for vertices of degree k will increase by k which means that the probability of these vertices being connected with large degree vertices is increasing and this corresponds to an assortative mixing⁸¹.

Rich-club

The rich-club property indicates the tendency of high degree vertices, to be connected to each other and forming clubs. It can be quantitatively measured as:

$$\phi(k) = \frac{2E_{>k}}{N_{>k}(N_{>k} - 1)} \quad (5)$$

Where $E_{>k}$ is the number of edges among the $N > k$ vertices and $N_{>k}$ is the number of vertices with degree larger than k . In order to obtain a more representative measure, the $\phi(k)$ of the network under study was normalized by dividing with the $\phi(k)$ of a random network with the same degree distribution as the network under study. This function is called $\rho_{ran}(k)$. If $\rho_{ran}(k)$ is an increasing function of k , the sub-networks containing vertices with degree larger than k will be denser as k increases and this implies the presence of a rich-club organization⁸².

Sensitive vertices and links

Given a scoring system for vertices, network hubs are defined as the vertices whose score is significantly higher than others ($> \text{mean} + 2 \times \text{SD}$). In this study, we used strength as the scoring system. Additionally, by defining a new score as the subtraction of the score of the network under study (in here the disease networks) from a reference network (in here the CN network), the activated regions in that network with respect to the reference network, is then computed as the vertices that their new score is significantly higher than others, respectively the deactivated regions are the ones that their new score is significantly lower. Further, by computing the absolute difference of the adjacency matrix of the network under study and the reference network, a scoring system for network edges was defined and likewise, the altered links were determined as edges that their score is significantly higher than others.

Data availability

Data collection and sharing for this project is funded by the Alzheimer's Disease Neuroimaging Initiative (ADNI) (National Institutes of Health, USA). The four main study networks are available in Supplementary Materials. All other intermediate data are available from the corresponding author upon request.

References

1. 2020 alzheimer's disease facts and fig. s. *Alzheimer's & Dementia* **16**, 391–460, DOI: <https://doi.org/10.1002/alz.12068>. <https://alz-journals.onlinelibrary.wiley.com/doi/pdf/10.1002/alz.12068>.
2. Organization, W. H. *Global Tuberculosis Report 2019*. Global tuberculosis control (World Health Organization, 2019).
3. Davis, M. *et al.* Estimating alzheimer's disease progression rates from normal cognition through mild cognitive impairment and stages of dementia. *Curr. Alzheimer research* **15**, 777–788 (2018).
4. Supekar, K., Menon, V., Rubin, D., Musen, M. & Greicius, M. D. Network analysis of intrinsic functional brain connectivity in alzheimer's disease. *PLoS Comput. Biol* **4**, e1000100 (2008).
5. Zhou, J. *et al.* Divergent network connectivity changes in behavioural variant frontotemporal dementia and alzheimer's disease. *Brain* **133**, 1352–1367 (2010).
6. Filippi, M. & Rocca, M. A. Clinical applications of the functional connectome. In *fMRI Techniques and Protocols*, 893–903 (Springer, 2016).
7. Bullmore, E. & Sporns, O. Complex brain networks: graph theoretical analysis of structural and functional systems. *Nat. reviews neuroscience* **10**, 186–198 (2009).
8. Bassett, D. S. & Sporns, O. Network neuroscience. *Nat. neuroscience* **20**, 353–364 (2017).
9. Betzel, R. F. *et al.* Changes in structural and functional connectivity among resting-state networks across the human lifespan. *Neuroimage* **102**, 345–357 (2014).
10. Tewarie, P. *et al.* Tracking dynamic brain networks using high temporal resolution meg measures of functional connectivity. *Neuroimage* **200**, 38–50 (2019).
11. Peer, M., Ron, Y., Monsa, R. & Arzy, S. Processing of different spatial scales in the human brain. *ELife* **8**, e47492 (2019).
12. Moerel, M., Yacoub, E., Gulban, O. F., Lage-Castellanos, A. & De Martino, F. Using high spatial resolution fmri to understand representation in the auditory network. *Prog. Neurobiol.* 101887 (2020).

13. Betzel, R. F. & Bassett, D. S. Multi-scale brain networks. *Neuroimage* **160**, 73–83 (2017).
14. Wu, Z. *et al.* Effects of brain parcellation on the characterization of topological deterioration in alzheimer's disease. *Front. aging neuroscience* **11**, 113 (2019).
15. Lang, E. W., Tomé, A. M., Keck, I. R., Górriz-Sáez, J. & Puntonet, C. G. Brain connectivity analysis: A short survey. *Comput. intelligence neuroscience* (2012).
16. Rossini, P. *et al.* Methods for analysis of brain connectivity: An ifcn-sponsored review. *Clin. Neurophysiol.* **130**, 1833–1858 (2019).
17. Bastos, A. M. & Schoffelen, J.-M. A tutorial review of functional connectivity analysis methods and their interpretational pitfalls. *Front. systems neuroscience* **9**, 175 (2016).
18. Sotiropoulos, S. N. & Zalesky, A. Building connectomes using diffusion mri: why, how and but. *NMR Biomed.* **32**, e3752 (2019).
19. Stephan, K. E. & Friston, K. J. Analyzing effective connectivity with functional magnetic resonance imaging. *Wiley Interdiscip. Rev. Cogn. Sci.* **1**, 446–459 (2010).
20. Wang, J., Zuo, X. & He, Y. Graph-based network analysis of resting-state functional mri. *Front. systems neuroscience* **4**, 16 (2010).
21. Van Den Heuvel, M. P. & Pol, H. E. H. Exploring the brain network: a review on resting-state fmri functional connectivity. *Eur. neuropsychopharmacology* **20**, 519–534 (2010).
22. Duda, J. T., Cook, P. A. & Gee, J. C. Reproducibility of graph metrics of human brain structural networks. *Front. neuroinformatics* **8**, 46 (2014).
23. Betzel, R. F., Bertolero, M. A. & Bassett, D. S. Non-assortative community structure in resting and task-evoked functional brain networks. *bioRxiv* 355016 (2018).
24. Grayson, D. S. *et al.* Structural and functional rich club organization of the brain in children and adults. *PLoS one* **9**, e88297 (2014).
25. Kim, D.-J. & Min, B.-K. Rich-club in the brain's macrostructure: Insights from graph theoretical analysis. *Comput. Struct. Biotechnol. J.* (2020).
26. Yin, C. *et al.* Network science characteristics of brain-derived neuronal cultures deciphered from quantitative phase imaging data. *Sci. reports* **10**, 1–13 (2020).
27. Xiang, J. *et al.* Graph-based network analysis of resting-state fmri: test-retest reliability of binarized and weighted networks. *Brain imaging behavior* **14**, 1361–1372 (2020).
28. van den Heuvel, M. P., Stam, C. J., Boersma, M. & Pol, H. H. Small-world and scale-free organization of voxel-based resting-state functional connectivity in the human brain. *Neuroimage* **43**, 528–539 (2008).
29. Bassett, D. S. & Bullmore, E. T. Small-world brain networks revisited. *The Neurosci.* **23**, 499–516 (2017).
30. Oldham, S. & Fornito, A. The development of brain network hubs. *Dev. cognitive neuroscience* **36**, 100607 (2019).
31. van den Heuvel, M. P. & Sporns, O. Network hubs in the human brain. *Trends cognitive sciences* **17**, 683–696 (2013).
32. Bertolero, M. A., Yeo, B. T. & D'Esposito, M. The modular and integrative functional architecture of the human brain. *Proc. Natl. Acad. Sci.* **112**, E6798–E6807 (2015).
33. Liu, J. *et al.* Complex brain network analysis and its applications to brain disorders: a survey. *Complexity* **2017** (2017).
34. Deco, G. & Kringelbach, M. L. Great expectations: using whole-brain computational connectomics for understanding neuropsychiatric disorders. *Neuron* **84**, 892–905 (2014).
35. Fornito, A. & Bullmore, E. T. Connectomics: a new paradigm for understanding brain disease. *Eur. Neuropsychopharmacol.* **25**, 733–748 (2015).
36. Hojjati, S. H. *et al.* Predicting conversion from mci to ad using resting-state fmri, graph theoretical approach and svm. *J. neuroscience methods* **282**, 69–80 (2017).
37. Castellanos, F. X., Di Martino, A., Craddock, R. C., Mehta, A. D. & Milham, M. P. Clinical applications of the functional connectome. *Neuroimage* **80**, 527–540 (2013).
38. Fornito, A., Zalesky, A. & Breakspear, M. The connectomics of brain disorders. *Nat. Rev. Neurosci.* **16**, 159–172 (2015).

39. Xue, C. *et al.* Disrupted patterns of rich-club and diverse-club organizations in subjective cognitive decline and amnesic mild cognitive impairment. *Front. neuroscience* **14** (2020).
40. He, Y., Chen, Z., Gong, G. & Evans, A. Neuronal networks in alzheimer's disease. *The Neurosci.* **15**, 333–350 (2009).
41. Sanz-Arigita, E. J. *et al.* Loss of 'small-world' networks in alzheimer's disease: graph analysis of fmri resting-state functional connectivity. *PloS one* **5**, e13788 (2010).
42. Zhao, X. *et al.* Disrupted small-world brain networks in moderate alzheimer's disease: a resting-state fmri study. *PloS one* **7**, e33540 (2012).
43. Buckner, R. L. *et al.* Cortical hubs revealed by intrinsic functional connectivity: mapping, assessment of stability, and relation to alzheimer's disease. *J. neuroscience* **29**, 1860–1873 (2009).
44. Sui, X. *et al.* Functional connectivity hubs could serve as a potential biomarker in alzheimer's disease: a reproducible study. *Curr. Alzheimer Res.* **12**, 974–983 (2015).
45. Bassett, D. S. & Siebenhühner, F. Multiscale network organization in the human brain. *Multiscale analysis nonlinear dynamics* 179–204 (2013).
46. Esteban, O. *et al.* fMRIPrep: a robust preprocessing pipeline for functional MRI. *Nat. Methods* DOI: [10.1038/s41592-018-0235-4](https://doi.org/10.1038/s41592-018-0235-4) (2018).
47. Esteban, O. *et al.* fmriprep. *Software* DOI: [10.5281/zenodo.852659](https://doi.org/10.5281/zenodo.852659) (2018).
48. Latora, V. & Marchiori, M. Efficient behavior of small-world networks. *Phys. review letters* **87**, 198701 (2001).
49. Barrat, A., Barthelemy, M. & Vespignani, A. *Dynamical processes on complex networks* (Cambridge university press, 2008).
50. Yeo, B. T. *et al.* The organization of the human cerebral cortex estimated by intrinsic functional connectivity. *J. neurophysiology* (2011).
51. Mowinckel, A. M. & Vidal-Piñeiro, D. Visualization of brain statistics with r packages ggseg and ggseg3d. *Adv. Methods Pract. Psychol. Sci.* **3**, 466–483 (2020).
52. Holten, D. Hierarchical edge bundles: Visualization of adjacency relations in hierarchical data. *IEEE Transactions on visualization computer graphics* **12**, 741–748 (2006).
53. Stanley, M. L. *et al.* Changes in brain network efficiency and working memory performance in aging. *PLoS One* **10**, e0123950 (2015).
54. Ma, X. *et al.* Enhanced network efficiency of functional brain networks in primary insomnia patients. *Front. psychiatry* **9**, 46 (2018).
55. Sha, Z. *et al.* Meta-connectomic analysis reveals commonly disrupted functional architectures in network modules and connectors across brain disorders. *Cereb. Cortex* **28**, 4179–4194 (2018).
56. Qian, S., Zhang, Z., Li, B. & Sun, G. Functional-structural degeneration in dorsal and ventral attention systems for alzheimer's disease, amnesic mild cognitive impairment. *Brain imaging behavior* **9**, 790–800 (2015).
57. Zhang, Z. *et al.* Functional degeneration in dorsal and ventral attention systems in amnesic mild cognitive impairment and alzheimer's disease: an fmri study. *Neurosci. letters* **585**, 160–165 (2015).
58. Bijsterbosch, J. *et al.* Challenges and future directions for representations of functional brain organization. *Nat. neuroscience* **23**, 1484–1495 (2020).
59. Ciric, R. *et al.* Benchmarking of participant-level confound regression strategies for the control of motion artifact in studies of functional connectivity. *NeuroImage* **154**, 174 – 187, DOI: <https://doi.org/10.1016/j.neuroimage.2017.03.020> (2017).
Cleaning up the fMRI time series: Mitigating noise with advanced acquisition and correction strategies.
60. Gorgolewski, K. *et al.* Nipype: a flexible, lightweight and extensible neuroimaging data processing framework in python. *Front. Neuroinformatics* **5**, 13, DOI: [10.3389/fninf.2011.00013](https://doi.org/10.3389/fninf.2011.00013) (2011).
61. Gorgolewski, K. J. *et al.* Nipype. *Software* DOI: [10.5281/zenodo.596855](https://doi.org/10.5281/zenodo.596855) (2018).
62. Tustison, N. J. *et al.* N4itk: Improved n3 bias correction. *IEEE Transactions on Med. Imaging* **29**, 1310–1320, DOI: [10.1109/TMI.2010.2046908](https://doi.org/10.1109/TMI.2010.2046908) (2010).
63. Avants, B., Epstein, C., Grossman, M. & Gee, J. Symmetric diffeomorphic image registration with cross-correlation: Evaluating automated labeling of elderly and neurodegenerative brain. *Med. Image Analysis* **12**, 26–41, DOI: [10.1016/j.media.2007.06.004](https://doi.org/10.1016/j.media.2007.06.004) (2008).

64. Zhang, Y., Brady, M. & Smith, S. Segmentation of brain MR images through a hidden markov random field model and the expectation-maximization algorithm. *IEEE Transactions on Med. Imaging* **20**, 45–57, DOI: [10.1109/42.906424](https://doi.org/10.1109/42.906424) (2001).
65. Dale, A. M., Fischl, B. & Sereno, M. I. Cortical surface-based analysis: I. segmentation and surface reconstruction. *NeuroImage* **9**, 179–194, DOI: [10.1006/nimg.1998.0395](https://doi.org/10.1006/nimg.1998.0395) (1999).
66. Klein, A. *et al.* Mindboggling morphometry of human brains. *PLoS Comput. Biol.* **13**, e1005350, DOI: [10.1371/journal.pcbi.1005350](https://doi.org/10.1371/journal.pcbi.1005350) (2017).
67. Fonov, V., Evans, A., McKinsty, R., Alml, C. & Collins, D. Unbiased nonlinear average age-appropriate brain templates from birth to adulthood. *NeuroImage* **47**, **Supplement 1**, S102, DOI: [10.1016/S1053-8119\(09\)70884-5](https://doi.org/10.1016/S1053-8119(09)70884-5) (2009).
68. Greve, D. N. & Fischl, B. Accurate and robust brain image alignment using boundary-based registration. *NeuroImage* **48**, 63–72, DOI: [10.1016/j.neuroimage.2009.06.060](https://doi.org/10.1016/j.neuroimage.2009.06.060) (2009).
69. Jenkinson, M., Bannister, P., Brady, M. & Smith, S. Improved optimization for the robust and accurate linear registration and motion correction of brain images. *NeuroImage* **17**, 825–841, DOI: [10.1006/nimg.2002.1132](https://doi.org/10.1006/nimg.2002.1132) (2002).
70. Power, J. D. *et al.* Methods to detect, characterize, and remove motion artifact in resting state fmri. *NeuroImage* **84**, 320–341, DOI: [10.1016/j.neuroimage.2013.08.048](https://doi.org/10.1016/j.neuroimage.2013.08.048) (2014).
71. Behzadi, Y., Restom, K., Liau, J. & Liu, T. T. A component based noise correction method (CompCor) for BOLD and perfusion based fmri. *NeuroImage* **37**, 90–101, DOI: [10.1016/j.neuroimage.2007.04.042](https://doi.org/10.1016/j.neuroimage.2007.04.042) (2007).
72. Satterthwaite, T. D. *et al.* An improved framework for confound regression and filtering for control of motion artifact in the preprocessing of resting-state functional connectivity data. *NeuroImage* **64**, 240–256, DOI: [10.1016/j.neuroimage.2012.08.052](https://doi.org/10.1016/j.neuroimage.2012.08.052) (2013).
73. Lanczos, C. Evaluation of noisy data. *J. Soc. for Ind. Appl. Math. Ser. B Numer. Analysis* **1**, 76–85, DOI: [10.1137/0701007](https://doi.org/10.1137/0701007) (1964).
74. Glasser, M. F. *et al.* A multi-modal parcellation of human cerebral cortex. *Nature* **536**, 171–178 (2016).
75. Sheng, J. *et al.* A novel joint hcpmmp method for automatically classifying alzheimer’s and different stage mci patients. *Behav. brain research* **365**, 210–221 (2019).
76. Khazaei, A., Ebrahimzadeh, A. & Babajani-Feremi, A. Application of advanced machine learning methods on resting-state fmri network for identification of mild cognitive impairment and alzheimer’s disease. *Brain imaging behavior* **10**, 799–817 (2016).
77. Liao, X., Vasilakos, A. V. & He, Y. Small-world human brain networks: perspectives and challenges. *Neurosci. & Biobehav. Rev.* **77**, 286–300 (2017).
78. Kawai, Y., Park, J. & Asada, M. A small-world topology enhances the echo state property and signal propagation in reservoir computing. *Neural Networks* **112**, 15–23 (2019).
79. Demaine, E. D. *et al.* Structural sparsity of complex networks: Bounded expansion in random models and real-world graphs. *J. Comput. Syst. Sci.* **105**, 199–241 (2019).
80. Humphries, M. D. & Gurney, K. Network ‘small-world-ness’: a quantitative method for determining canonical network equivalence. *PloS one* **3**, e0002051 (2008).
81. Newman, M. E. Assortative mixing in networks. *Phys. review letters* **89**, 208701 (2002).
82. Colizza, V., Flammini, A., Serrano, M. A. & Vespignani, A. Detecting rich-club ordering in complex networks. *Nat. physics* **2**, 110–115 (2006).

Acknowledgments

This work has been supported in part by a grant from the Cognitive Sciences and Technologies Council with grant No. 8226. In addition, the second author is indebted to the Research Core: “Bio-Mathematics with computational approach” of Tarbiat Modares University, with Grant No IG-39706.

Author contributions statement

A. Fathian: Conceptualization, Data curation, Formal analysis, Investigation, Methodology, Software, Validation, Visualization, Writing – original draft, Writing – review and editing; Y. Jamali: Supervision, Conceptualization, Formal analysis, Investigation, Methodology, Project administration, Resources, Software, Validation, Review and editing; M. R. Raoufy: Validation, Review and editing

Competing Interests Statement

The authors declare no competing financial interests.

Figures

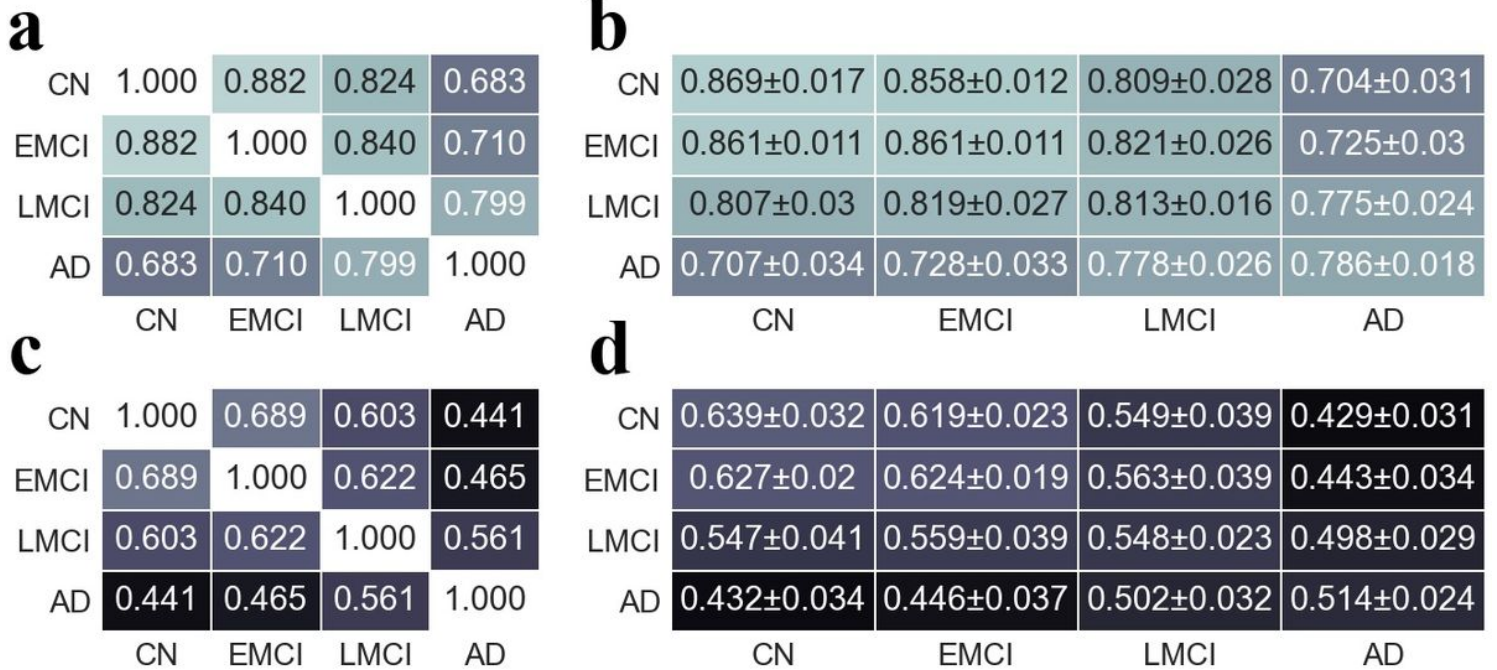


Figure 1

The similarity between study groups follows a trend proportional to the trend of disease progression. (a) The PCC between the four main study networks. (b) For each study group, the 23 subjects of each group were randomly divided into two subgroups of 11 and 12 networks. Then, the mean networks of these 12 and 11 subjects were constructed, and the PCC between these two mean networks was computed. This process was repeated 100 times resulting in 100 PCC matrices. This panel shows the element-wise mean and SD of these matrices. (c) The Jaccard similarity coefficient among the four main study networks. (d) Similar to the panel (b) but for the Jaccard similarity coefficient.

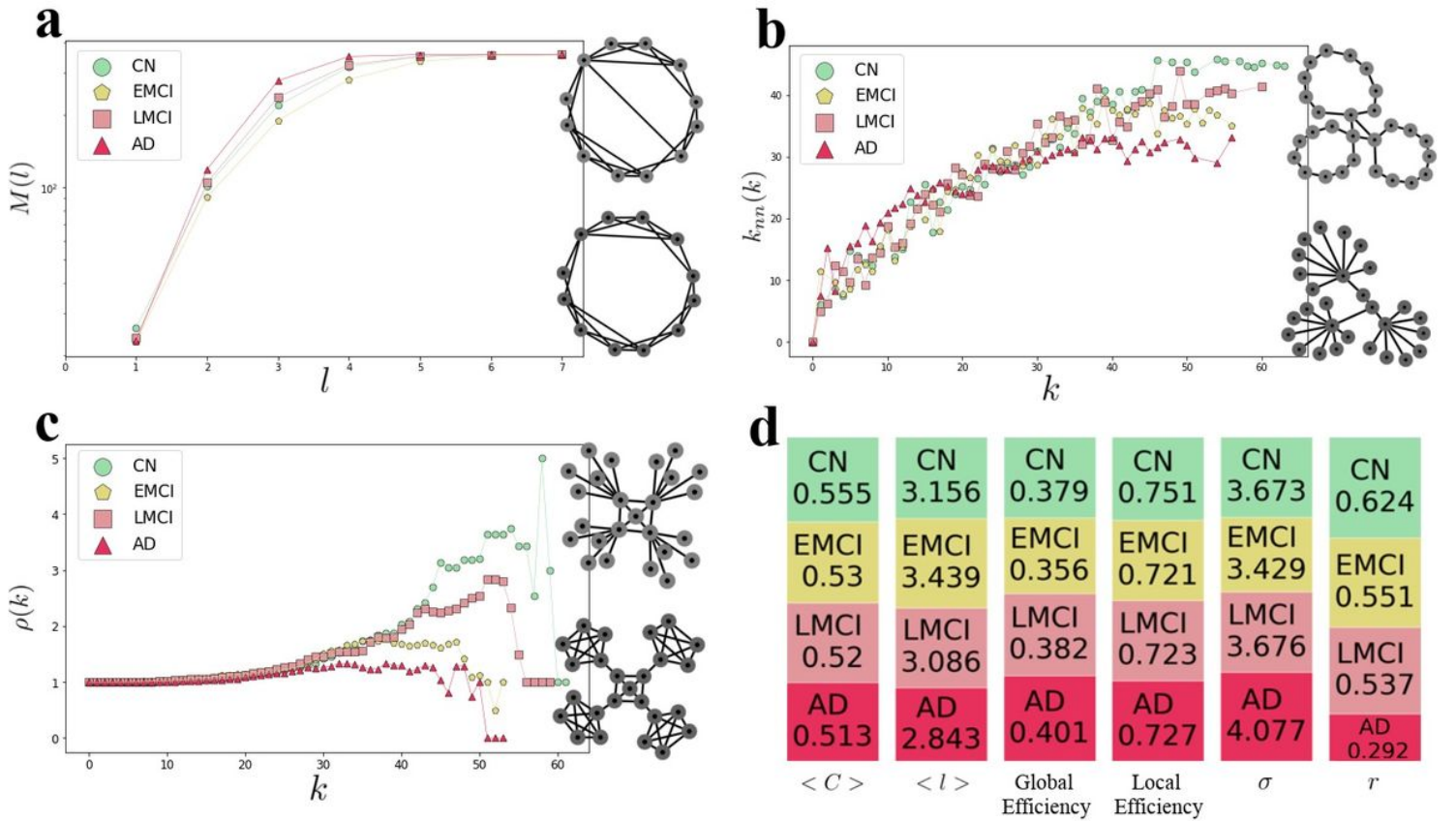


Figure 2

The emergence of the small-worldness, assortativity, and rich-club phenomenon in the study networks. (a) $M(l)$ plot showing the average number of vertices within a distance less than or equal to l from any given vertex is almost increased by the disease progression and suggests that the study networks have the small-world property that is almost stronger in the disease networks. Two graphs on the right-hand side are toy examples demonstrating the increase in the randomness of network connections (from bottom to top), which leads to the increase in the emergence of the small-world property. (b) $Knn(k)$ plot showing the average degree of the nearest neighbors, for vertices of degree k , is almost decreased by the disease progression and suggests that the study networks have assortative architecture and this assortative matching follows a decreasing trend proportional to the disease progression. Two graphs on the right-hand side are toy examples of assortative (top) and disassortative (bottom) networks. (c) $\rho(k)$ plot showing the amount of inter-connectivity among vertices of degree higher than k is almost decreased by the disease progression and suggests that the rich-club phenomenon is disappearing by the disease progression. Two graphs on the right-hand side are toy examples of networks with (top) and without (bottom) rich-club. (d) The bar plots showing $\langle C \rangle$, $\langle l \rangle$, global efficiency, local efficiency, σ (normalized $\langle C \rangle$ / normalized $\langle l \rangle$), and r (PCC between the degrees of all vertices at either ends of an edge).

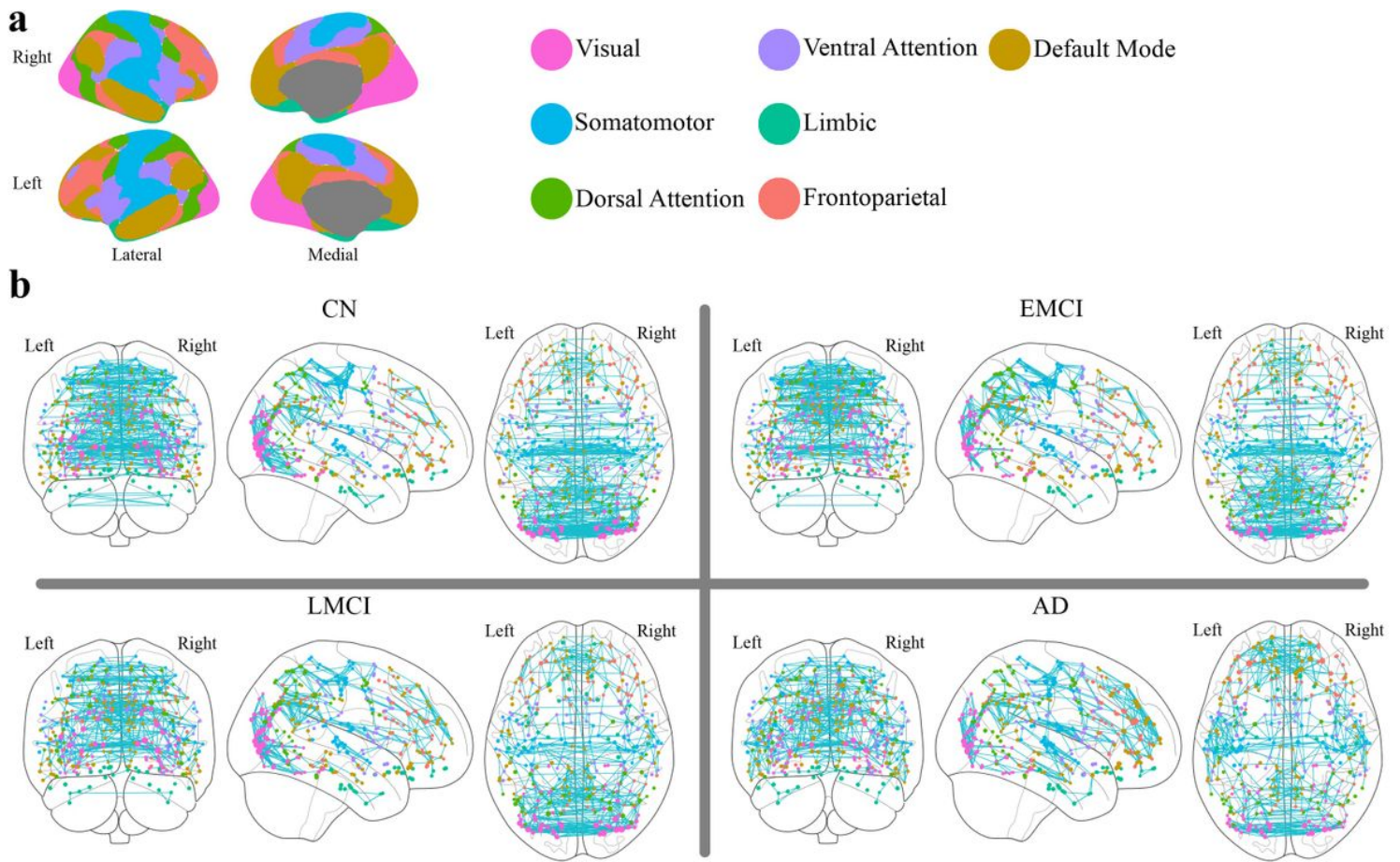
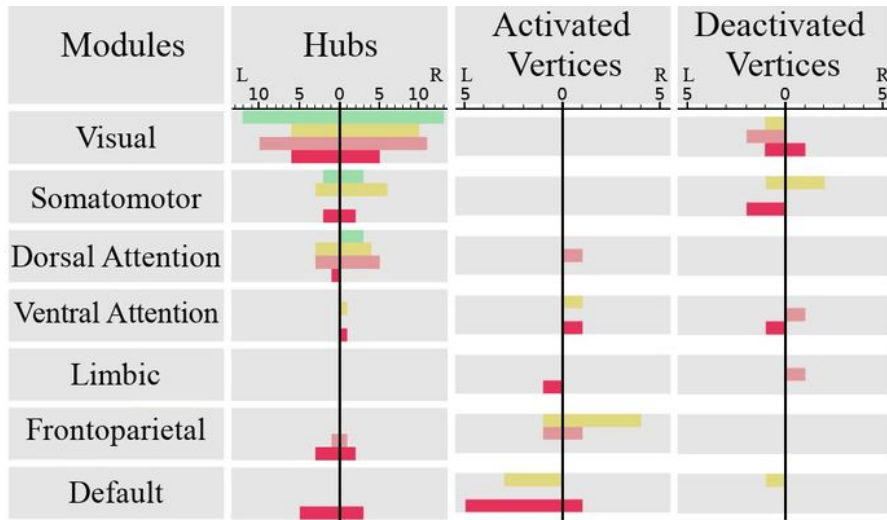


Figure 3

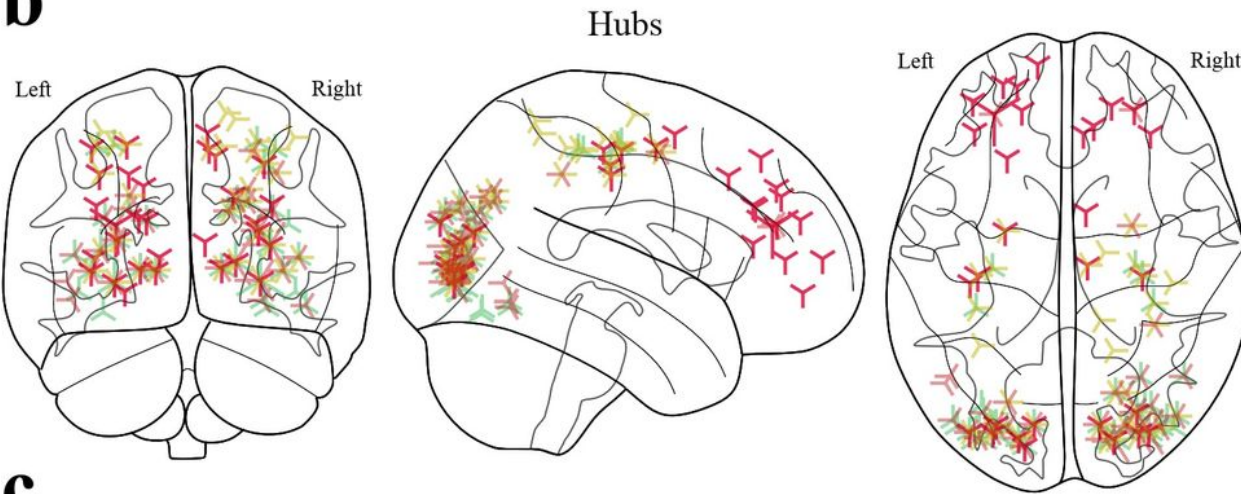
The overall gradually changing patterns of highly-weighted links are following a trend proportional to the disease progression. (a) The spatial distribution of the 7-module parcellation (made with “ggseg” R package⁵¹). (b) The top 1 percent highly-weighted links of each study network. Vertex color represents the module the vertex belongs to, and the vertex size is proportional to the vertex strength. It shows that there is a trend towards the increase in the number of default mode links as well as the intra-hemisphere links in limbic. It also shows a trend towards the decrease in the inter-hemisphere links in limbic and dorsal attention.

Legends

a



b



c

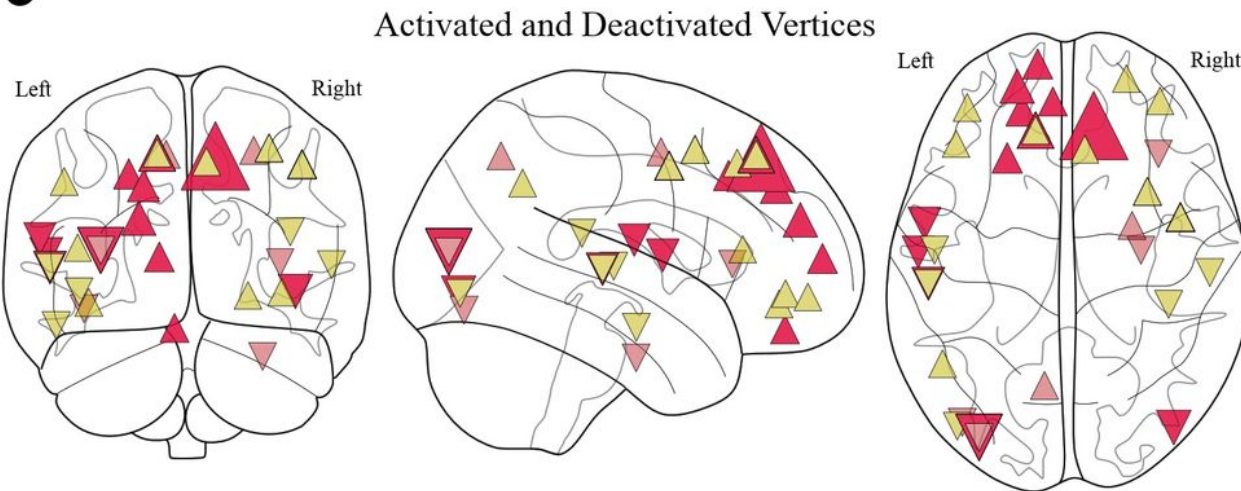


Figure 4

The distribution of hubs, activated areas, and deactivated areas shows that anterior regions are more engaged in the diseased groups. (a) The frequency distribution across the 7-module parcellation. The left and right sides of each sub-plot denoted by a vertical black line represent the distribution across modules limited to the left and right hemispheres, respectively (b) The spatial distribution of the hub regions. The vertex size is proportional to the vertex strength. (c) The spatial distribution of vertices that are activated

(denoted by 4) and deactivated (denoted by 5) in the diseases. A vertex was called activated (deactivated) with respect to disease if the subtraction of its strength in the disease network from the CN network was significantly larger (smaller) than the similar value for other vertices. The vertex size is proportional to the value of this subtraction.

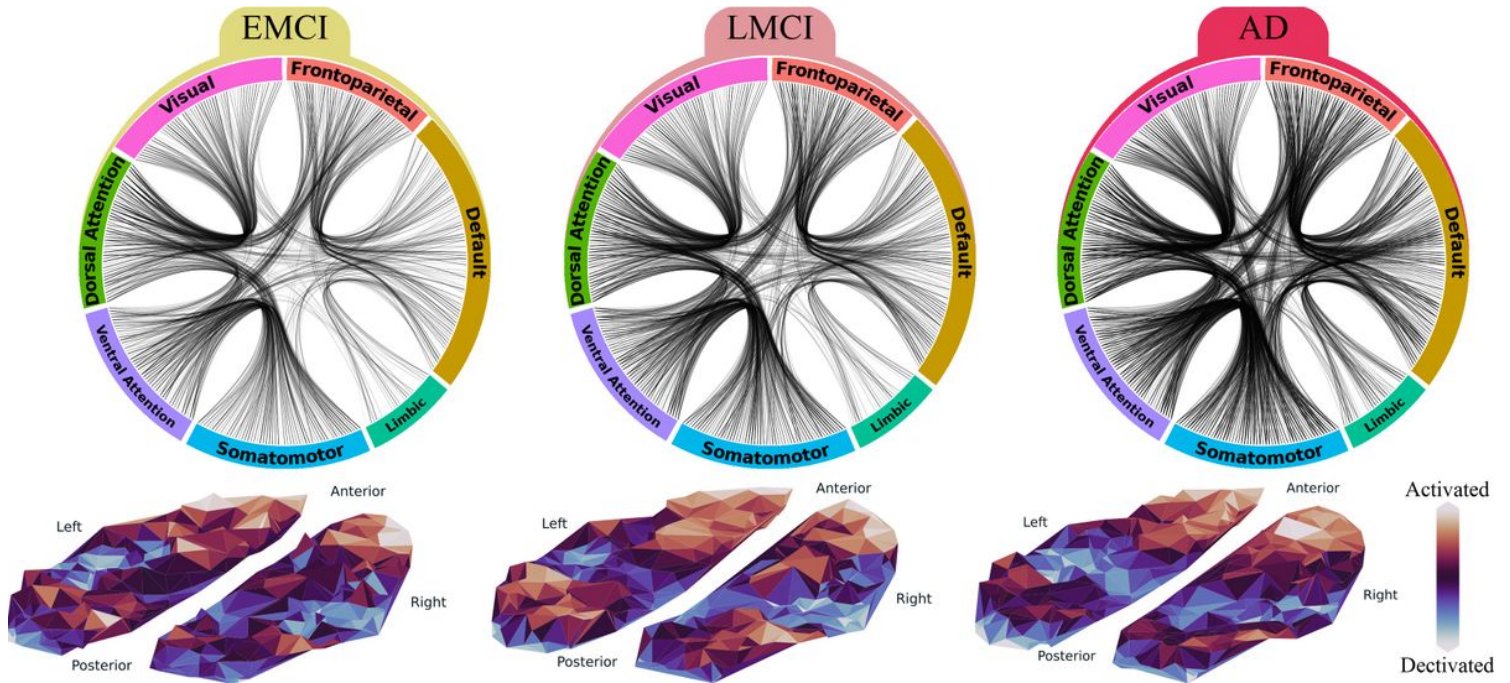


Figure 5

The alterations in the brain functional network induced by the disease stages. For each disease stage the connectogram of the links with significantly different weights as compared to the CN group is depicted in the top row. It shows a similar inter-module connectivity pattern is repeating through all disease stages. The altered links with respect to disease are defined as the significantly larger or smaller elements of the matrix results from the subtraction of the disease network from the CN network. Diagrams are plotted based on the Hierarchical Edge Bundling algorithm⁵², which allows bundling the intra-module edges together to get a more elegant presentation. The bottom row indicates the alterations in the vertices' strength by showing the top-view spatial distribution of the activated or deactivated vertices similar to Fig. 4c.

Supplementary Files

This is a list of supplementary files associated with this preprint. Click to download.

- [SupportingInformation.pdf](#)
- [studynetworksdata.zip](#)